On the Spectral Curvature of VHE Blazar 1ES 1011+496: Effect of Spatial Particle Diffusion

Atreyee Sinha[1], S. Sahayanathan[2], B. S. Acharya[1], G. C. Anupama[3], V. R. Chitnis[1], and B. B. Singh[1]
[1] Department of High Energy Physics, Tata Institute of Fundamental Research, Homi Bhabha Road, Mumbai 400005, India; atreyee@tifr.res.in
[2] Nuclear Research Laboratory, Bhabha Atomic Research Center, Mumbai, India
[3] Indian Institute of Astrophysics, II Block, Koramangala, Bangalore, 560 034, India

Abstract

A detailed multi-epoch study of the broadband spectral behavior of the very high energy (VHE) source 1ES 1011 +496 provides us with valuable information regarding the underlying particle distribution. Simultaneous observations of the source at optical/UV/X-ray/γ-ray during three different epochs, as obtained from *Swift*-UVOT/*Swift*-XRT/*Fermi*-LAT, are supplemented with the information available from the VHE telescope array, HAGAR. The long-term flux variability at the *Fermi*-LAT energies is clearly found to be lognormal. It is seen that the broadband spectral energy distribution of 1ES 1011+496 can be successfully reproduced by synchrotron and synchrotron self Compton emission models. Notably, the observed curvature in the photon spectrum at X-ray energies demands a smooth transition of the underlying particle distribution from a simple power law to a power law with an exponential cutoff, or a smooth broken power law distribution, which may possibly arise when the escape of the particles from the main emission region is energy dependent. Specifically, if the particle escape rate is related to its energy as $E^{0.5}$, then the observed photon spectrum is consistent with the ones observed during the various epochs.

Key words: BL Lacertae objects: individual (1ES 1011+496) – galaxies: active – radiation mechanisms: non-thermal

1. Introduction

Blazars are a peculiar subclass of radio loud active galactic nuclei where a powerful relativistic jet is pointed close to the line of sight of the observer (Urry & Padovani 1995). They show high optical polarization, intense and highly variable non-thermal radiation throughout the entire electromagnetic spectra in timescales extending from minutes to years, apparent superluminal motion in high resolution radio maps, large Doppler factors, and beaming effects. Blazars can be broadly classified into two subgroups, BL Lacs and flat spectrum radio quasars (FSRQs), where the former are identified by the absence of emission/absorption lines. The broadband spectral energy distribution (SED) of blazars is characterized by two peaks, one in the IR–X-ray regime, and the second one in the γ-ray regime. According to the location of the first peak, BL Lacs are further classified into low energy peaked BL lacs (LBLs), intermediate energy peaked BL Lacs (IBLs), and high energy peaked BL Lacs (HBLs; Padovani & Giommi 1995). Both leptonic (e.g., Maraschi et al. 1992; Dermer & Schlickeiser 1993; Sikora et al. 1994; Bloom & Marscher 1996; Błażejowski et al. 2000) and hadronic (e.g., Mannheim & Biermann 1992; Mücke & Protheroe 2001; Mücke et al. 2003) models have been proposed to explain the broadband SED with varying degrees of success. While the origin of the low energy component is well established to be caused by synchrotron emission from relativistic electrons gyrating in the magnetic field of the jet, the physical mechanisms responsible for the high energy emission are still under debate. It can be produced either via inverse Compton scattering (IC) of low frequency photons by the same electrons responsible for the synchrotron emission (leptonic models), or via hadronic processes initiated by relativistic protons, neutral and charged pion decays, or muon cascades (hadronic models). The seed photons for IC in leptonic models can be either the source synchrotron photons

(synchrotron self Compton, SSC) or from external sources such as the broad line region, the accretion disc, the cosmic microwave background, and so on (external Compton, EC). For a comprehensive review of these mechanisms, see Böttcher (2007).

1ES 1011+496 (R.A. = 10:15:04.14, decl. = 49:26:00.70; J2000) is an HBL located at a redshift of $z = 0.212$. It was discovered as a very high energy (VHE) emitter by the MAGIC collaboration in 2007, following an optical outburst in March 2007 (Albert et al. 2007). The flux above 200 GeV was roughly 7% of the Crab Nebula, and the observed spectrum was reported to be a power law with a very steep index of 4.0 ± 0.5. After correction for attenuation of VHE photons by the extragalactic background light (EBL; Kneiske & Dole 2010), the intrinsic spectral index was computed to be 3.3 ± 0.7. At its epoch of discovery, it was the most distant TeV source. Albert et al. (2007) had constructed the SED with simultaneous optical R-band data, and other historical data from Costamante & Ghisellini (2002), and modeled it with a single zone radiating via SSC processes. However, the model parameters could not be constrained due to the sparse sampling and the non-simultaneity of the data. Hartman et al. (1999) had suggested the association of this source with the EGRET source 3EG J1009+4855, but this association has later been challenged (Sowards-Emmerd et al. 2003). This source has been detected in the 0.1–300 GeV band by *Fermi*-LAT, and in the 0.3–10 keV band by *Swift*-XRT (Abdo et al. 2010). A detailed study of its optical spectral variability has been performed by Böttcher et al. (2010). Results of multiwavelength campaigns carried out in 2008 (Ahnen et al. 2016b) and 2011–2012 (Aleksić et al. 2016) have recently been published by the MAGIC collaboration.

In 2014 February, 1ES 1011+496 was reported to be in its highest flux state to date, as seen by *Fermi*-LAT (Corbet & Shrader 2014) and *Swift*-XRT (Kapanadze 2014). During this
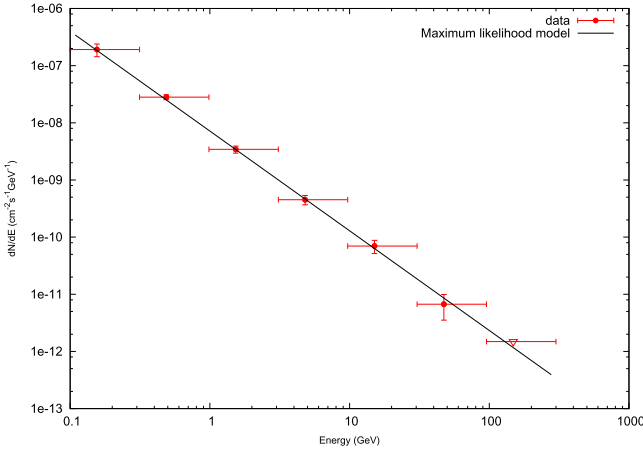
Figure 1. Energy spectrum of 1ES1 1011+496 from 6 years of *Fermi*-LAT data during 2008–2014. The last point is an upper limit and is shown by an inverted triangle. The spectrum is well fit by a power law of index $\alpha = 1.82 \pm 0.01$.

time, the VERITAS collaboration also detected a strong VHE flare from this source, at an integral flux level of $\sim$20%–75% of the Crab flux, which was almost a factor of 10 higher than its baseline flux (Cerruti 2015). Ahnen et al. (2016a) have used the TeV spectrum during this flare to put constraints on the EBL density. This source was observed by the High Altitude Gamma-Ray (HAGAR) Telescope array during the 2014 February–March season. In this paper, we study the simultaneous SED of this source, as seen by *Swift*, *Fermi*-LAT, and HAGAR during this epoch. To understand the broadband spectral behavior, we also construct SEDs using quasi-simultaneous data from two previous epochs.

In Section 2, we describe our data reduction procedure and study the temporal variability in the lightcurves. The distribution function of the flux at the γ-ray energies is studied in Section 3. We model the SED using an SSC model having a smoothly varying power law spectrum of the underlying electron energy distribution, and the results are outlined in Section 4. We discuss the implications in Section 5, and show that such a situation may arise when the escape of the particles from the emission region is energy dependent. The results are summarized in Section 6. A cosmology with $\omega_m = 0.3$, $\omega_\Lambda = 0.7$, and $H_0 = 70$ km s^{-1} Mpc is used in this work.

2. Data Analysis and Lightcurves

2.1. Fermi-LAT

Fermi-LAT data are extracted from a region of $20°$ centered on the source. The standard data analysis procedure as mentioned in the *Fermi*-LAT documentation[4] is used. Events belonging to the energy range $0.2-300$ GeV and SOURCE class are used. To select good time intervals, a filter "DATA_QUAL>0," && "LAT_CONFIG==1" is used, and only events with less than $105°$ zenith angle are selected to avoid contamination from the Earth limb γ-rays. The galactic diffuse emission component gll_iem_v05_rev1.fits and an isotropic component iso_source_v05_rev1.txt are used as the background models. The unbinned likelihood method included in the pylikelihood library of Science Tools (v9r33p0) and the post-launch instrument response

functions P7REP_SOURCE_V15 are used for the analysis. All the sources lying within a $10°$ region of interest (ROI) centered at the position of 1ES 1011+496 and defined in the third *Fermi*-LAT catalog (Acero et al. 2015) are included in the XML file. All the parameters except the scaling factor of the sources within the ROI are allowed to vary during the likelihood fitting. The source spectrum is assumed to be a power law.

Analysis of all data for this source from 2008 to 2014 yields a spectrum consistent with a simple power law with an index of 1.82 ± 0.01 (Figure 1), and the flux is found to be variable on a timescale of 10 days, with a significance of 12.7σ. The fractional variability amplitude parameter (Vaughan et al. 2003; Chitnis et al. 2009) is computed to be $F_{\mathrm{var}} = 0.35 \pm 0.01$, where

$$F_{\mathrm{var}} = \sqrt{\frac{S^2 - \sigma_{\mathrm{err}}^2}{\bar{x}^2}}. \tag{1}$$

Here σ_{err}^2 is the mean square error, $\bar{x}$ the unweighted sample mean, and S^2 the sample variance, and the error on F_{var} is given as

$$\sigma_{F_{\mathrm{var}}} = \sqrt{\left(\sqrt{\frac{1}{2N}} \cdot \frac{\sigma_{\mathrm{err}}^2}{\bar{x}^2 F_{\mathrm{var}}}\right)^2 + \left(\sqrt{\frac{\sigma_{\mathrm{err}}^2}{N}} \cdot \frac{1}{\bar{x}}\right)^2}, \tag{2}$$

with N as the number of points.

There is no significant trend of spectral hardening with increasing flux (Spearman's rank correlation, $rs = -0.25$), which has been seen in many HBL. The light curve for a 3-year period during 2011–2014 is shown in the bottom panel of Figure 2.

Spectra are extracted in five logarithmically binned energy bins for three epochs contemporaneous with *Swift* observations, corresponding to MJD (a) 56005 to 56020 (state s1), (b) 56280 to 56310 (state s2), and (c) 56692 to 56720 (state s3). LAT fluxes and spectral parameters during these epochs are given in Table 1. The state s3 corresponds to the period for which the highest gamma-ray flux from this source is seen to date.

2.2. Swift-XRT

A total of 16 *Swift* pointings are available during the studied epochs, the ids of which are given in Table 1. *Swift*-XRT data (Burrows et al. 2005) are processed with the XRTDAS software package (v.3.0.0) available within the HEASOFT package (6.16). Event files are cleaned and calibrated using standard procedures (xrtpipeline v.0.13.0), and xrtproducts v.0.4.2 is used to obtain the lightcurves and spectra. Observations are available in both Windowed Timing (WT) and Photon Counting (PC) modes, and full grade selections (0–2 for WT and 0–12 for PC) are used. PC observations during the 2014 flare are heavily piled up (counts >0.5 c/s), and are corrected for by following the procedure outlined in the *Swift* analysis threads.[5] The XRT Point Spread Function is modeled by a King function,

$$\mathrm{PSF}(r) = [1 + (r/r_c)^2]^{-\beta}, \tag{3}$$

with $r_c = 5.8$ and $\beta = 1.55$ (Moretti et al. 2005). Depending on the source brightness, annular regions are chosen to exclude pixels deviating from the King's function. The tool xrtmkarf
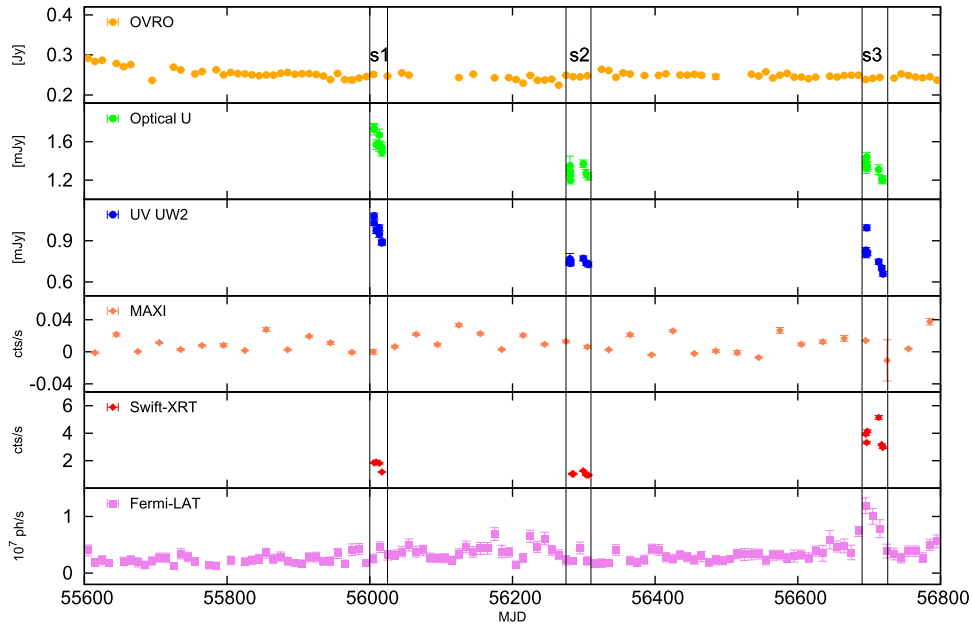

Figure 2. Multiwavelength light curve during MJD 55600 to 56800 (calendar days 2011–2014), showing from top: Panel 1: OVRO flux in Jy; Panel 2: Optical U band flux in mJy; Panel 3: UV flux in UW2 band in mJy; Panel 4: MAXI flux (with monthly binning) in counts/sec; Panel 5: *Swift*-XRT flux in counts/sec; Panel 6: *Fermi*-LAT flux (with 10 days binning) in ph cm^{-2} s^{-1}. The three states for which SED has been studied are marked and labelled as s1, s2, and s3, respectively.

is then executed with PSF correction set to "yes" to create an ARF corrected for the loss of counts due to the exclusion of this central region. For example, for observation id 00035012032 (see Figure 4), an annular region of 16–25 arcsec centered on the source position is taken as the source region.

The lightcurves are finally corrected for telescope vignetting and PSF losses with the tool `xrtlccorr v.0.3.8`. The spectra are combined using the tool `addspec` for all observations within each of the states s1, s2, and s3, as defined in Section 2.1. Spectra are grouped to ensure a minimum of 30 counts in each bin by using the tool `grppha v.3.0.1`.

A slight curvature is detected in the XRT spectrum, and a log parabolic spectral model given by

$$dN/dE = K(E/E_b)^{-\alpha - \beta \log(E/E_b)}, \qquad (4)$$

is used to model the observed spectrum. Here α gives the spectral index at E_b, which is fixed at 1 keV during the fitting. Parameters obtained during the fitting are given in Table 1. To correct for the line of sight absorption of soft X-rays due to the interstellar gas, the neutral hydrogen column density is fixed at $N_H = 8.38 \times 10^{19}$ cm^{-2} (Kalberla et al. 2005).

2.3. Swift-UVOT

Swift-UVOT observations cycled through the six filters, the optical U, V, B, and the UV UW1, UW2, and UM2. The individual exposures during each of the states are summed using `uvotimsum v.1.6`, and the `uvotsource v.3.3` tool is used to extract the fluxes from the images using aperture photometry. The observed fluxes are corrected for galactic extinction using the dust maps of Schlegel et al. (1998), and for contribution from the host galaxy following Nilsson et al. (2007), with R-mag = 16.41 ± 0.09.

2.4. Other Multiwavelength Data

We supplement the previous information with other multiwavelength flux measurements at different energies:

(i) *Radio.*

As a part of the Fermi monitoring program, the Owens Valley Radio Observatory (OVRO; Richards et al. 2011) has been regularly observing this source since 2008. Flux measurements at 15 GHz taken directly from their website[6] show negligible variability with $f_{var} \sim 0.07$.

(ii) *X-ray.*

Daily binned source counts in the 2–20 keV range from the Monitor of All-sky X-ray Image (MAXI) on board the International Space Station (ISS; Matsuoka et al. 2009) are available from their website.[7] The X-ray counts binned on monthly timescales show high variability, with $f_{var} = 1.34 \pm 0.08$.

(iii) *VHE.*

HAGAR (Gothe et al. 2013) is a hexagonal array of seven Atmospheric Cherenkov Telescopes (ACT) that uses the wavefront sampling technique to detect celestial gamma-rays. It is located at the Indian Astronomical Observatory site (32°46′46″ N, 78°58′35″ E), in Hanle, Ladakh, in the Himalayan mountain ranges, at an altitude of 4270 m. The energy threshold for the HAGAR array for vertically incident γ-ray showers is 208 GeV, with a sensitivity of detecting a Crab Nebula–like source in 17 hr for a 5σ significance. Detailed descriptions of HAGAR instrumentation and simulations can be found in Shukla et al. (2012) and Saha et al. (2013). HAGAR observations of 1ES 1011+496 were carried out during the 2014 February–March season following an alert by MAGIC and VERITAS collaborations of a VHE flare from this source during February 3–11 (Mirzoyan 2014).

Table 1
Observation Details (XRT Observation Ids and the Total Exposure Time) and Spectral Parameters in the X-ray and GeV Bands
for the Different States for which the SED Has Been Extracted

State	Start Date ISO	End Date ISO	XRT Obs id	XRT Exp Time (ks)	XRT Spectral Parameters			LAT Spectral Parameters	
					α	β	$F_{2-10\,\mathrm{keV}}$	Index	$F_{0.2-300\,\mathrm{GeV}}$
s1	2012 Mar 19	2012 Apr 03	00035012020 00035012021 00035012022 00035012023 00035012024	6.3	2.27 ± 0.19	0.17 ± 0.10	1.6 ± 0.3	1.81 ± 0.16	4.3 ± 0.9
s2	2012 Dec 19	2013 Jan 18	00035012025 00035012026 00035012027 00035012028 00035012029 00035012030	5.1	2.37 ± 0.11	0.61 ± 0.22	0.82 ± 0.07	1.74 ± 0.13	2.8 ± 0.6
s3	2014 Feb 04	2014 Mar 04	00035012031 00035012032 00035012033 00035012035 00035012036	7.3	1.94 ± 0.04	$0.16 \pm 0.0.03$	4.11 ± 0.12	1.77 ± 0.22	9.8 ± 0.3

Note. The X-ray 2–10 keV flux is quoted in 10^{-11} erg cm^{-2} s^{-1}, and the *Fermi*-LAT 0.2–300 GeV Flux in 10^{-8} ph cm^{-2} s^{-1}.

The observations were carried out in clear moonless conditions, between 2014 February 19 and March 8 (MJD 56707 to 56724). Each pointing source (ON) run of approximately 60 minutes duration was followed (or preceded) by a background (OFF) run of the the same time duration at the same zenith angle, having similar night sky brightness as the source region. A total of 23 run pairs were taken, corresponding to a total duration of 1035 minutes with a common ON–OFF hour angle.

The data are reduced following the procedures outlined in Shukla et al. (2012), with various quality cuts imposed. Only events with signals seen in at least five telescopes are retained, for which the energy threshold is calculated to be 234 GeV. No significant signal is seen from the source with 600 minutes of clean data. The excess of signal over background is computed to be 706 ± 566 photons, corresponding to a significance of 1.3σ. A $3-\sigma$ upper limit of $1.2 * 10^{-10}$ erg cm^{-2} s^{-1} for the flux of gamma-rays above 234 GeV is calculated from the previously provided data, which corresponds to roughly 70% of the Crab Nebula flux.

This is supplemented with VHE spectra of this source obtained during its epoch of discovery (Albert et al. 2007) by the Major Atmospheric Gamma-ray Imaging Cherenkov (MAGIC). These spectral points have been plotted for representative purposes in Figure 5 and provide a lower limit for the SED modeling during the VHE flare in 2014, epoch s3.

3. Detection of Lognormality

Lognormal flux distributions and linear rms-flux relations have often been claimed as universal features of accretion powered sources like X-ray binaries (Uttley & McHardy 2001; Scaringi et al. 2012). Lognormal fluxes have fluctuations that are, on average, proportional to the flux itself, and are indicative of an underlying multiplicative, rather than additive, physical process. It has been suggested that a lognormal flux behavior in blazars could be indicative of the variability imprint of the accretion disk onto the jet (McHardy 2008). This behavior in

blazars was first clearly detected in the X-ray regime in BL Lac (Giebels & Degrange 2009) and has hence been seen across the entire electromagnetic spectrum in PKS 2155−304 (Chevalier et al. 2015) and Mkn 421 (Sinha et al. 2016).

Since for the present source the variability is minimal in the MAXI and OVRO bands, and the sampling sparse in the UVOT and XRT bands, we restrict our study of lognormal flux variability to the Fermi band only. We fit the histogram of the observed fluxes with a Gaussian and a lognormal function (Figure 3(a)), and find that a lognormal fit (chi-sq/dof = 11/12) is statistically preferred over a Gaussian fit (chi-sq/dof = 22.8/12). We further plot the excess variance, $\sigma_{\mathrm{EXCESS}} = \sqrt{S^2 - \sigma_{\mathrm{err}}^2}$, versus the mean flux in Figure 3(b). The two parameters show a strong linear correlation, r (prob) = 76% (1.6e–5), and are well fit by a straight line of slope 1.17 ± 0.18 and an intercept of $(-3.9 \pm 0.8) \times 10^{-8}$ (chi-sq/dof = 24.1/22). This indicates a clear detection of lognormal temporal behavior in this source.

4. Spectral Energy Distribution

The broadband SED of 1ES 1011+496, during different activity states, is modeled under the ambit of a simple leptonic scenario. This, in turn, helps us understand the the nature of the electron distribution responsible for the emission through synchrotron and SSC processes. We assume the electrons to be confined within a spherical zone of radius R permeated by a tangled magnetic field B. As a result of the relativistic motion of the jet, the radiation is Doppler boosted along the line of sight. A good sampling of the SED from radio to γ-rays allows one to obtain a reasonable estimation of the physical parameters, under appropriate assumptions (Ghiselini et al. 1996; Tavecchio et al. 1998; Sahayanathan & Godambe 2012). Notably, the smooth spectral curvatures, observed around the peak of the SED, may result from a convolution of the single particle emissivity with the assumed particle distribution. If the chosen particle distribution has a sharp break, then the observed curvature in the photon
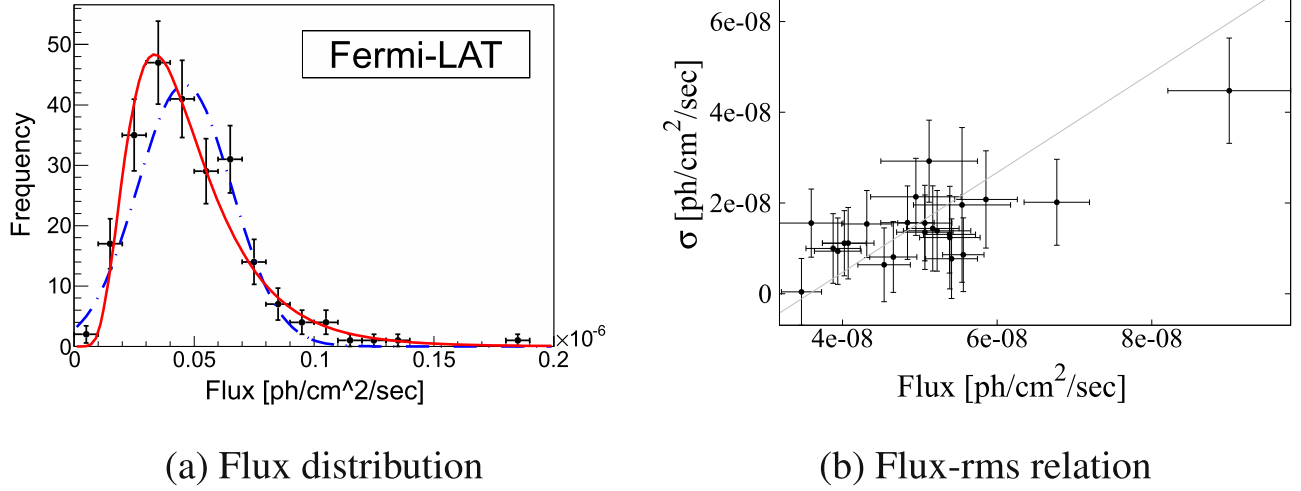
(a) Flux distribution

(b) Flux-rms relation

Figure 3. Detection of lognormality in 1ES 1011+496 in the Fermi energy band. The first panel shows the histogram of the observed fluxes (black points) fitted with a Gaussian (dotted blue line) and lognormal (solid red line) function. A lognormal fit is clearly preferred. The second panel shows the strong linear relationship between the flux and the excess rms. The black points denote data points averaged over 100 days, and the solid gray line indicates the linear fit.
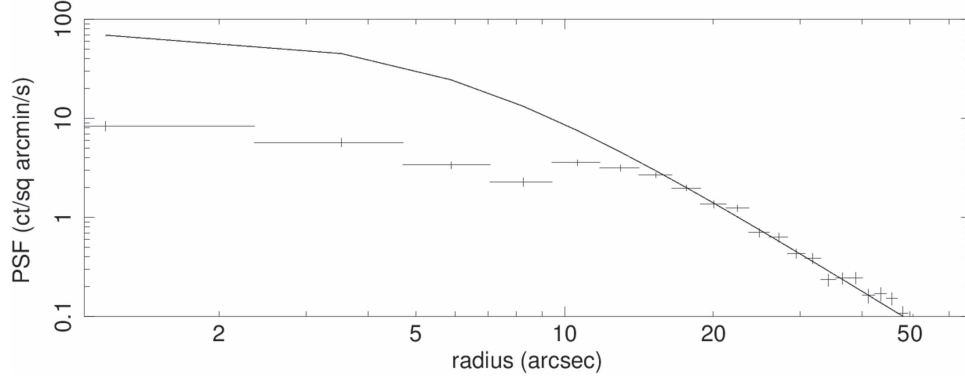
Figure 4. XRT PSF for obs 00035012032 fitted by a King function. The deviation from the model is seen for regions smaller than 16 arcsec, which are thus excluded from the source region.

spectrum could be due to the emissivity function. On the other hand, the underlying particle distribution itself can show a gradual transition causing the observed curvatures. To investigate this, the observed SED is modeled with the following choices of particle distributions.

(i) *Broken power law (BPL).* In this case, we assume the electron spectrum to be a sharp BPL with indices p and q, given by

$$N(\gamma)d\gamma = \begin{cases} N_0\gamma^{-p}d\gamma, & \gamma_{\min} < \gamma < \gamma_b \\ N_0\gamma_b^{(q-p)}\gamma^{-q}d\gamma, & \gamma_b < \gamma < \gamma_{\max} \end{cases}. \quad (5)$$

(ii) *Smooth broken power law (SBPL).* Here the electron distribution is an SBPL with low energy index p and the high energy index q:

$$N(\gamma)d\gamma = N_0\frac{(\gamma_b)^{-p}}{(\gamma/\gamma_b)^p + (\gamma/\gamma_b)^q}d\gamma, \, \gamma_{\min} < \gamma < \gamma_{\max}. \quad (6)$$

(iii) *Power law with an exponential cutoff (CPL).* The particle distribution in this case is chosen to be a power

law with index p and an exponentially decreasing tail, given by

$$N(\gamma)d\gamma = N_0\gamma^{-p}\exp\left(-\frac{\gamma}{\gamma_c}\right)d\gamma, \, \gamma_{\min} < \gamma < \gamma_{\max}. \quad (7)$$

Here, $\gamma_{\min}$ and $\gamma_{\max}$ are the minimum and maximum dimensionless energies ($E = \gamma mc^2$) of the non-thermal electron distribution, and γ_b is the electron energy associated with the peak of the SED and N_0 the normalization. To reduce the number of unknowns, the radius R is fixed at 1.3×10^{16} cm, corresponding to a variability timescale of $t_{\text{var}} \approx 1$ day (for the Doppler factor $\delta \approx 10$). In addition, the magnetic field energy density, $U_B \left(= \frac{B^2}{8\pi}\right)$, is considered to be in near equipartition with the particle energy density (U_e). The resultant model spectra, corresponding to epoch s3, for the previously provided three choices of particle distribution are shown in Figure 6, along with the observed fluxes. The governing physical parameters are given in Table 2.

We compare the different fit models by incorporating the numerical SSC model into the XSPEC spectral fitting software to perform a χ^2 minimization as followed in Sinha et al. (2016).

Table 2
Models Parameters, the Total Bolometric Luminosity (L) and the Computed Reduced-χ^2 for the Different Particle Distributions during the Three Epochs. while the BPL Cannot Reproduce the Observed Spectrum Satisfactorily, the SBPL and the CPL Can

	Broken Power Law (BPL)							
State	Particle Index		Magnetic Field	Doppler Factor	Break Energy	Particle Energy Density	Luminosity	χ^2/dof
	p	q	B (G)	δ	γ_b	U_e (erg/cc)	L (erg/cc)	
s1	2.35	4.20	0.82	10.0	7.7e4	5.1e-2	3.2e46	10.3
s2	2.20	4.60	0.78	10.2	8.1e4	3.8e-2	2.6e46	9.4
s3	2.26	4.30	0.73	9.8	1.9e5	7.4e-2	7.7e46	12.1
	Smooth Broken Power Law (SBPL)							
	p	q	B (G)	δ	γ_b	U_e (erg/cc)	L (erg/cc)	
s1	2.35	4.22	0.83	10.0	9.5e4	7.8e-2	3.7e46	1.3
s2	2.20	4.60	0.78	10.2	7.7e4	4.7e-2	2.3e46	1.1
s3	2.22	4.20	0.73	9.8	1.7e5	8.6e-2	7.8e46	1.2
	Cutoff Power Law (CPL)							
		p	B (G)	δ	γ_{max}	U_e (erg/cc)	L (erg/cc)	
s1		2.30	0.78	10.9	1.1e5	8.2e-2	3.4e46	1.2
s2		2.02	0.76	10.7	7.0e4	4.6e-2	2.1e46	1.4
s3		2.10	0.74	10.3	1.6e5	8.6e-2	6.6e46	1.3
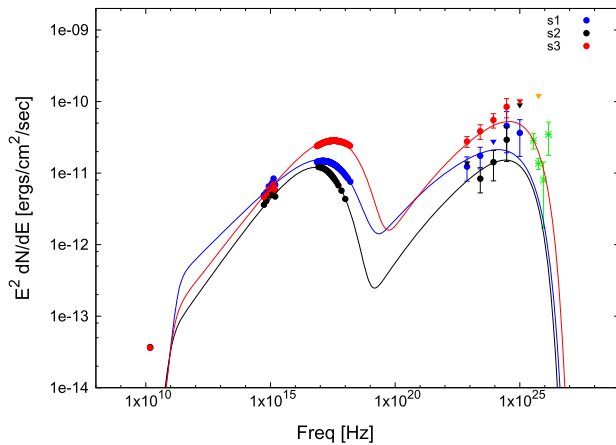
(a) Cutoff power law
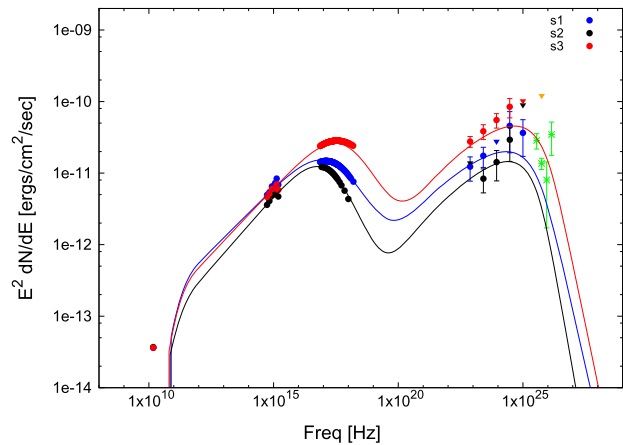
(b) Smooth broken power law

Figure 5. Spectral energy distribution of 1ES 1011+496 during the three epochs studied in the paper, with simultaneous data from *Swift*-UVOT, *Swift*-XRT, and the *Fermi*-LAT. The orange inverted triangle gives the HAGAR upper limit during the 2014 February–March season. The green stars show the MAGIC spectrum during its discovery in 2007 (Albert et al. 2007). The SEDs are modeled with a one zone SSC, with the underlying electron distribution as (a) a power law with exponential cutoff and (b) a smooth broken power law.

Swift-XRT is binned to have eight spectral points to avoid biasing the fit toward X-ray energies. Since we are dealing with several different instruments over a broad energy range, we assume model systematics of 5%. Our study shows that the commonly used electron spectrum, the BPL (e.g., Ghisellini et al. 1996; Krawczynski et al. 2004), cannot explain the smooth curvature observed at the X-ray energies for this source, implying that the synchrotron emissivity function alone is not sufficient to give rise to the observed curvature, and that the underlying particle spectrum itself must have a gradual transition as opposed to a sharp break. This suggests that the SBPL and CPL are the better choices to represent the observed SED, and in Figure 5 we show the model spectra corresponding to these particle distributions for all three epochs considered in this study. Both these models can well reproduce the observed spectrum, during all three epochs, and the absence of high energy X-ray/simultaneous TeV measurements prevents us

from distinguishing between the two models. Particularly, with the current sampling, the index q and the γ_{max} for the SBPL cannot be well constrained, and the latter is fixed at 10^7. The model parameters describing the observed SED for the three epochs for the SBPL and the CPL are also listed in Table 2.

The different flux states can be reproduced mainly by changing the particle indices and the break energy, whereas the variations in other parameters like the Doppler factor and the magnetic field are minimal. While the total bolometric luminosity, L, changes by more than a factor of three, the variations in B and δ are less than 10%. This probably suggests that the variation in the flux states may occur mainly due to changes in the underlying particle distributions, rather than the other jet properties.

5. Discussions

The observations of lognormality in the long term (6 years) gamma-ray flux distribution and the linear flux-rms relation
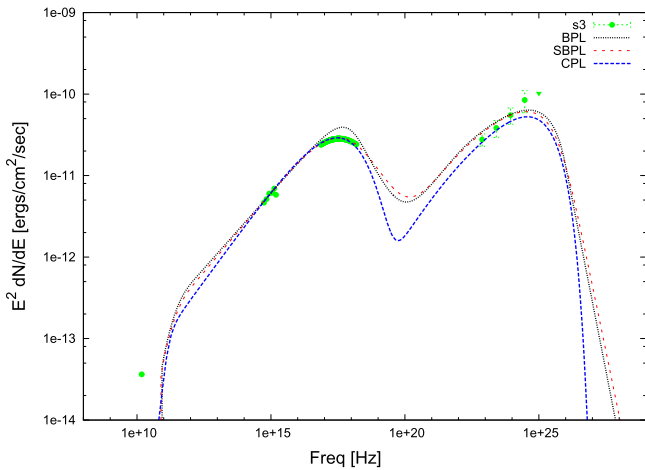
Figure 6. State s3 modeled with the underlying spectrum as a BPL (dotted black line); a SBPL (dashed red line); and a CPL (dashed blue line). The BPL fails to reproduce the smooth curvature of the observed SED (shown in green).

Figure 7. Model curves obtained by changing the energy dependence of the escape timescale for the state s3. The blue line is obtained for a energy independent escape ($\xi = 0$), and fails to reproduce the observed spectrum. The best match between the data and the model is obtained for $\xi = -0.5$ and is represented by the solid green line. The magnetic field B is assumed to be 0.4 G and the Doppler factor $\delta = 10$. The injected particle spectrum is a power of index 2.1.

imply that the γ-ray flux variability of 1ES 1011+496 is lognormal. Since similar trends have been seen in the X-ray band in sources like the Seyfert 1 galaxy; Mkn 766 (Vaughan et al. 2003), where the physical process responsible for the X-ray emission originates in the galactic disc; and other compact accreting systems like cataclysmic variables (Giannios 2013), such trends have been claimed as universal signs of accretion induced variability. The other option might be that the underlying parameters responsible for the observed emission (e.g., the Doppler factor, magnetic field, etc.) themselves have a lognormal time dependence (Giebels & Degrange 2009). Since the result of our spectral modeling indicates that the flux variability is mainly induced by changes in the particle spectrum rather than the other jet properties, it seems reasonable to believe that lognormal fluctuations in the accretion rate give rise to an injection rate into the jet with similar properties.

Moreover, a detailed study of the multiwavelength spectral behavior of the source during three different epochs under simple synchrotron and SSC models demands an underlying electron distribution with a smooth curvature. Though such a requirement can be satisfied by assuming the underlying electron distribution as either SBPL or CPL, the absence of hard X-ray data prevents one from distinguishing between these two choices. To interpret this, we consider a scenario where a non-thermal distribution of electrons $Q(\gamma) = Q_0 \gamma^{-p}$ is continuously injected into a cooling region (CR) where they lose their energy through radiative processes as well as escape out at a rate defined by a characteristic timescale, t_{esc}. The evolution of the particle number density, $N(\gamma, t)$, in the CR can then be conveniently described by the kinetic equation (Kardashev 1962)

$$\frac{\partial N}{\partial t} - \frac{\partial}{\partial \gamma}(P(\gamma)N) + \frac{N}{t_{esc}(\gamma)}$$
$$= Q(\gamma)\Theta(\gamma - \gamma_{min})\Theta(\gamma_{max} - \gamma), \quad (8)$$

where $P(\gamma)$ is the energy loss rate due to synchrotron and SSC processes. Assuming a power law dependence of escape timescale with energy $t_{esc} = \tau\gamma^\xi$, a semianalytical solution of Equation (8) can be attained when the loss processes are confined within the Thomson regime (Atoyan & Aharonian 1999). However, detection of the source
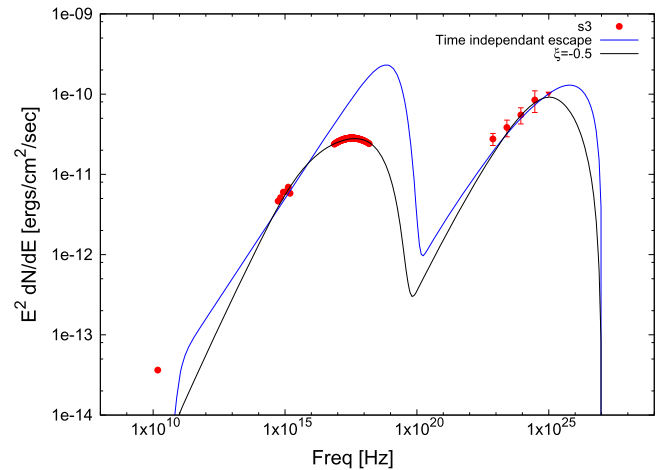
at VHE energies suggests that the Thomson scattering approximation of SSC process may not be valid and one needs to incorporate Klein–Nishina correction in the cross-section (Tavecchio et al. 1998). Hence, we numerically solve Equation (8) using a fully implicit finite difference scheme (Chang & Cooper 1970; Chiaberge & Ghisellini 1999), while incorporating the exact Klein–Nishina cross-section for IC scattering (Blumenthal & Gould 1970).

The case $t_{esc} \rightarrow \infty$ (no escape) gives rise to a BPL with the break occurring at the energy where the observation time is equal to the cooling timescale of the particle, while for the case $\xi = 0$ (constant t_{esc}), a steady state BPL particle distribution is eventually attained where the break corresponds to the particle energy at which the escape timescale equates to its cooling timescale. However, in these cases, the spectral transition at the break energy is too sharp to reproduce the observed SED, and a gradual transition can be achieved by considering $\xi \neq 0$. We found that the smooth spectral curvature demanded by the observation can be attained by fixing $\xi \approx 0.5$. In Figure 7, we show the resultant model SED corresponding to $\xi = 0$ (blue line) and $\xi = 0.5$, along with the observed fluxes for the state s3. The underlying particle distribution corresponding to these values of ξ is shown in Figure 8.

Alternate to this interpretation, a smooth curvature in the particle distribution can also be a result of time averaging of an evolving particle distribution. For instance, an episodic injection of a power-law particle distribution into CR can cause the high energy cutoff to shift toward lower energy with time, which will be reflected as a smooth curvature at high energy in the time averaged spectrum. Also, an episodic injection with an energy-dependent escape gives rise to a particle distribution similar to a cutoff power law. However, this interpretation fails to explain the observed variability of the gamma-ray flare, since the observed cooling timescale of the GeV gamma-ray emitting electrons will come out to be (Kushwaha et al. 2014)

$$t_{cool,GeV} \approx 3 \times 10^{10} B^{-7/4} \left(\frac{\delta}{\nu_{GeV}}\right)^{1/4} s \quad (9)$$

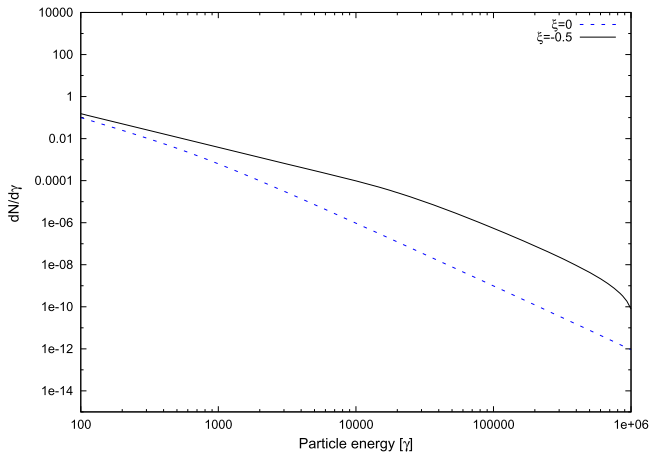$$\approx 0.5 \text{ days.} \quad (10)$$

Figure 8. Underlying particle spectra for the model curves shown in Figure 7. The dashed blue line is obtained for an energy independent escape ($\xi = 0$; which fails to reproduce the observed SED), and the solid black line corresponds to the particle spectrum that best models the observed SED ($\xi = -0.5$).

Here the cooling timescale is estimated for the parameters provided in Table 2, and $\nu_{\rm GeV}$ corresponds to the frequency of the gamma-ray photon falling on the Compton peak. This time is much smaller than the observed flare duration of ≈ 30 days, as seen in Figure 2. Similarly, the particle spectrum injected into the CR itself can show smooth curvatures, due to an underlying complex particle acceleration prices. For example, an energy-dependent acceleration process is known to give rise to significant curvature in the accelerated particle distribution (Massaro et al. 2004; Zirakashvili & Aharonian 2007). However, in this present work, we only consider a simplistic scenario where the smooth curvature can be introduced by considering an energy-dependent escape from the main emission region.

6. Conclusions

The blazar, 1ES 1011+496, underwent a major γ-ray flare during 2014 February, triggering observations at other wavebands, thereby providing simultaneous observations of the source at radio/optical/X-ray/γ-ray energies. The TeV flare seen by VERITAS on 2014 February 3–11 decayed down by 2014 February 19, as indicated by the HAGAR upper limits. This is also seen in the flux decrease in the Fermi and the X-ray bands. In this work, we analyzed the simultaneous multi-wavelength spectrum of the source and obtained the broadband SED during three different epochs. The observed SEDs over these epochs clearly show a trend of the synchrotron peak moving to higher energies during increased flux states, similar to the "bluer when brighter" trend seen by Böttcher et al. (2010) during 5 years of optical observations of this source. However, Böttcher et al. (2010) attributed the observed variability primarily due to magnetic field changes in the jet, whereas our broadband spectral modeling results indicate the spectral behavior is dominated by changes in the particle spectrum.

The spectra during all the states demand a smooth curvature in the underlying particle spectrum (e.g., an SBPL or a CPL). We show that such a smoothly varying particle spectrum can be easily obtained by assuming an energy-dependent particle escape ($t_{\rm esc} \propto \gamma^{\xi}$) mechanism in the jet. The inferred injected

particle power law index $p \sim 2.1$ indicates that the particles are most likely accelerated at relativistic shocks (Sironi et al. 2015). However, the non-availability of hard X-ray observation presently prevents us from distinguishing between CPL and SBPL particle spectra. Future observations in the hard X-ray band from the newly launched ASTROSAT (Singh et al. 2014) can be crucial in resolving this uncertainty.

The detection of lognormal flux variability in this source follows similar recent detections in other blazars. While the γ-ray flux distribution could be modeled by a single lognormal distribution for other HBLs (Mkn421; Sinha et al. 2016 and PKS2155-304; Chevalier et al. 2015), the FSRQ PKS 1510-089 (Kushwaha et al. 2016) required a sum of two such distributions. With the Fermi mission now into its ninth year of operation, we have unprecedented continuous flux measurements for a large sample of blazars. A systematic study of the same can shed new light on the origin of the jet launching mechanisms in supermassive blackholes.

References

Abdo, A. A., Ackermann, M., Agudo, I., et al. 2010, ApJ, 716, 30
Acero, F., Ackermann, M., Ajello, M., et al. 2015, ApJS, 218, 23
Ahnen, M. L., Ansoldi, S., Antonelli, L. A., et al. 2016a, A&A, 590, A24
Ahnen, M. L., Ansoldi, S., Antonelli, L. A., et al. 2016b, MNRAS, 459, 2286
Albert, J., Aliu, E., Anderhub, H., et al. 2007, ApJL, 667, L21
Aleksić, J., Ansoldi, S., Antonelli, L. A., et al. 2016, A&A, 591, A10
Atoyan, A. M., & Aharonian, F. A. 1999, MNRAS, 302, 253
Błażejowski, M., Sikora, M., Moderski, R., & Madejski, G. M. 2000, ApJ, 545, 107
Bloom, S. D., & Marscher, A. P. 1996, ApJ, 461, 657
Blumenthal, G. R., & Gould, R. J. 1970, RvMP, 42, 237
Böttcher, M. 2007, Ap&SS, 309, 95
Böttcher, M., Hivick, B., Dashti, J., et al. 2010, ApJ, 725, 2344
Burrows, D. N., Hill, J. E., Nousek, J. A., et al. 2005, SSRv, 120, 165
Cerruti, M. 2015, arXiv:1501.03554
Chang, J. S., & Cooper, G. 1970, JCoPh, 6, 1
Chevalier, J., Kastendieck, M. A., Rieger, F., et al. 2015, ICRC, 34, 829
Chiaberge, M., & Ghisellini, G. 1999, MNRAS, 306, 551
Chitnis, V. R., Pendharkar, J. K., Bose, D., et al. 2009, ApJ, 698, 1207
Corbet, R. H. D., & Shrader, C. R. 2014, ATel, 5888, 1
Costamante, L., & Ghisellini, G. 2002, A&A, 384, 56
Dermer, C. D., & Schlickeiser, R. 1993, ApJ, 416, 458
Ghisellini, G., Maraschi, L., & Dondi, L. 1996, A&AS, 120, C503
Giannios, D. 2013, MNRAS, 431, 355
Giebels, B., & Degrange, B. 2009, A&A, 503, 797

Gothe, K. S., Prabhu, T. P., Vishwanath, P. R., et al. 2013, ExA, 35, 489
Hartman, R. C., Bertsch, D. L., Bloom, S. D., et al. 1999, ApJS, 123, 79
Kalberla, P. M. W., Burton, W. B., Hartmann, D., et al. 2005, A&A, 440, 775
Kapanadze, B. 2014, ATel, 5866, 1
Kardashev, N. S. 1962, SvA, 6, 317
Kneiske, T. M., & Dole, H. 2010, A&A, 515, A19
Krawczynski, H., Hughes, S. B., Horan, D., et al. 2004, ApJ, 601, 151
Kushwaha, P., Chandra, S., Misra, R., et al. 2016, ApJL, 822, L13
Kushwaha, P., Sahayanathan, S., Lekshmi, R., et al. 2014, MNRAS, 442, 131
Mannheim, K., & Biermann, P. L. 1992, A&A, 253, L21
Maraschi, L., Ghisellini, G., & Celotti, A. 1992, ApJL, 397, L5
Massaro, E., Perri, M., Giommi, P., & Nesci, R. 2004, A&A, 413, 489
Matsuoka, M., Kawasaki, K., Ueno, S., et al. 2009, PASJ, 61, 999
McHardy, I. 2008, in Blazar Variability across the Electromagnetic Spectrum,
    Workshop Proc. (Trieste: PoS), 14
Mirzoyan, R. 2014, ATel, 5887, 1
Moretti, A., Campana, S., Mineo, T., et al. 2005, Proc. SPIE, 5898, 360
Mücke, A., & Protheroe, R. J. 2001, APh, 15, 121
Mücke, A., Protheroe, R. J., Engel, R., Rachen, J. P., & Stanev, T. 2003, APh,
    18, 593

Nilsson, K., Pasanen, M., Takalo, L. O., et al. 2007, A&A, 475, 199
Padovani, P., & Giommi, P. 1995, ApJ, 444, 567
Richards, J. L., Max-Moerbeck, W., Pavlidou, V., et al. 2011, ApJS, 194, 29
Saha, L., Chitnis, V. R., Vishwanath, P. R., et al. 2013, APh, 42, 33
Sahayanathan, S., & Godambe, S. 2012, MNRAS, 419, 1660
Scaringi, S., Körding, E., Uttley, P., et al. 2012, MNRAS, 421, 2854
Schlegel, D. J., Finkbeiner, D. P., & Davis, M. 1998, ApJ, 500, 525
Shukla, A., Chitnis, V. R., Vishwanath, P. R., et al. 2012, A&A, 541, A140
Sikora, M., Begelman, M. C., & Rees, M. J. 1994, ApJ, 421, 153
Singh, K. P., Tandon, S. N., Agrawal, P. C., et al. 2014, Proc. SPIE,
    9144, 1
Sinha, A., Shukla, A., Saha, L., et al. 2016, A&A, 591, A83
Sironi, L., Keshet, U., & Lemoine, M. 2015, SSRv, 191, 519
Sowards-Emmerd, D., Romani, R. W., & Michelson, P. F. 2003, ApJ,
    590, 109
Tavecchio, F., Maraschi, L., & Ghisellini, G. 1998, ApJ, 509, 608
Urry, C. M., & Padovani, P. 1995, PASP, 107, 803
Uttley, P., & McHardy, I. M. 2001, MNRAS, 323, L26
Vaughan, S., Edelson, R., Warwick, R. S., & Uttley, P. 2003, MNRAS, 345, 1271
Zirakashvili, V. N., & Aharonian, F. 2007, A&A, 465, 695